Biophysical Journal, Volume 99

Supporting Material

Mapping dynamic protein interactions to insulin secretory granule behavior with TIRF-FRET

Alice D Lam, Sahar Ismail, Ray Wu, Ofer Yizhar, Daniel R Passmore, Stephen A Ernst, and Edward L Stuenkel

SUPPORTING MATERIAL

MATERIALS AND METHODS:

Cell culture and transfection

MIN6 cells were cultured in 5% CO_2, in DMEM containing 4.5g/L glucose and glutamine (Gibco, Carlsbad, CA), supplemented with 15% fetal bovine serum, penicillin (50U/mL), streptomycin (50μg/mL), and 0.0005% β-mercaptoethanol. Cells were transfected with Lipofectamine 2000 (Invitrogen), according to the manufacturer's protocol. For imaging experiments, cells were plated onto poly-L-lysine coated #1.5 thickness coverslips 36-48 hours prior to use, and transfected 16-18 hours before imaging.

Molecular biology and generation of recombinant DNA constructs

All fluorescent constructs used monomeric versions of the fluoroproteins CFP, cerulean (a CFP mutant that exhibits a higher extinction coefficient and higher quantum yield) (1), cYFP (a YFP derivative that exhibits reduced pH sensitivity and longer Forster distance) (2-3) and cherry. A linked cYFP-cerulean construct was generated by ligating sequence coding for cerulean onto the C-terminal end of cYFP, with a 15 amino acid linker (SGLRSRDPLALPVAT). The cYFP-cerulean FRET constructs fused to PH or VAMP2 sequences were made by ligating VAMP2 (rat, gift from Richard Scheller, Stanford University) or the PH domain of PLC delta (gift from Kees Jalink, Netherlands Cancer Institute), to the C-terminal end of the cYFP-cerulean sequence (with a flexible 11 amino acid linker (SGFSGGSGGSG). Single fluorophore-labeled PH and VAMP2 constructs were generated from these constructs via restriction digests and ligations that removed either the cYFP or cerulean coding regions. To generate N-terminal fluoroprotein-labeled constructs of Rab27A (human, Missouri S&T cDNA Resource Center) and Slp4A (rat, gift from Romano Regazzi, University of Lausanne), the respective cDNAs were subcloned into the SalI-XbaI sites of pDNR-dual for use with the Cre recombinase-mediated Creator System (Clontech, Mountain View, CA) and recipient vectors pLoxP-ECFP-C1, pLoxP-Cerulean-C1, pLoxP-cYFP-C1. Mutants of Rab27A (Q78L, T23N) and Slp4A (AG) (mutation of TGDWFY to AGAAAY, amino acid positions 115-120) were constructed in the pDNR vector using polymerase chain reaction-based Quickchange Site-Directed Mutagenesis kit from Stratagene (Cedar Creek, TX). NPY-Cherry was constructed by ligating sequence coding for Cherry onto the C-terminal end of NPY (gift from Ron Holz, University of Michigan). The sequence fidelity of all constructs was confirmed by DNA sequencing (University of Michigan DNA Sequencing Core).

Purification of bacterially expressed proteins

E. coli (strains BL21 DE3, JM109) expressing His-tagged cYFP, CFP, and cYFP-CFP were a gift from Joel Swanson (University of Michigan). Cells were grown to an OD of 0.4-0.6, induced with 0.1mM isopropyl β-D-1-thiogalactopyranoside (IPTG), grown for 7 hours at 30C, and centrifuged (15 minutes, 5000g, Beckman JA-14 rotor). Pelleted cells were resuspended in equilibration buffer (50mM Na_2HPO_4, 300mM NaCl, 0.5% Triton X-100, pH 7.0, with protease inhibitors (G-Biosciences, St. Louis, MO)), and lysed with a French press at 15000psi. Cell lysates were solubilized by shaking on ice for 1 hour, followed by centrifugation to remove insoluble debris (20 minutes, 20,000g, Beckman JA-20 rotor). His-tagged proteins were purified from cell lysates with TALON metal affinity resin beads (Clontech, Mountain View, CA)

according to the manufacturer's protocol. Following binding of His-tagged proteins to the TALON beads, the beads were rinsed in wash buffer (50mM Na_2HPO_4, 300mM NaCl, pH 7.0, with 5mM imidazole), and the protein was eluted from the beads in wash buffer with 150mM imidazole. Protein purity was determined using fractionation by SDS-PAGE and Coomassie staining and estimated to be ~90%. Prior to use in conjugation reactions, proteins were dialyzed into a coupling buffer.

Conjugation of fluoroproteins to silica beads/coverslips

Fluoroproteins were conjugated to 10µm silica beads (Discovery Scientific, Vancouver, Canada) or to glass coverslips (1.5 thickness, Warner Instruments, Hamden, CT). The surfaces were amino-silylated for 30 seconds in a 2% solution of 3-aminopropyltriethoxysilane (Pierce Biotechnology, Rockford, IL) in acetone, then rinsed with acetone. Fluoroproteins were crosslinked to this surface using a Sulfo-LC-SPDP cross-linker (Pierce Biotechnology). Proteins were first passed through a 0.22µm filter to remove insoluble debris, and equilibrated into coupling buffer (50mM Na_2HPO_4, 150mM NaCl, 10mM EDTA, 0.02% NaN_3, pH 7.2) by overnight dialysis at 4C using 3.5K Slide-a-Lyzer cassettes (Pierce Biotechnology). Equilibrated protein was diluted to ~ 0.6mg/mL in coupling buffer for the crosslinking reaction. Sulfo-LC-SPDP crosslinker was added to the protein solution to a final concentration of 1mM, and the reaction proceeded in the dark (25C, 30-60 minutes). Free crosslinker was removed from the protein solution by dialysis into coupling buffer (4C, 12 hours) using 3.5K Slide-a-Lyzer cassettes. The amino-silylated glass surfaces were separately modified with Sulfo-LC-SPDP crosslinker, by covering the surfaces in a solution of 1mM Sulfo-LC-SPDP in coupling buffer (25C, 30-60 minutes). The modified glass surfaces were rinsed in coupling buffer, and bound crosslinker was reduced by treatment with 50mM DTT in coupling buffer (25C, 30 minutes), followed by rinsing with coupling buffer. The Sulfo-LC-SPDP modified protein solutions were added to the modified and reduced glass surfaces, and the crosslinking reaction proceeded in the dark with shaking (4C, 18 hours). The protein-modified glass surfaces were rinsed in coupling buffer and stored at 4C in coupling buffer prior to use. Visual inspection of the surfaces under fluorescence microscopy demonstrated that the fluoroprotein-modification of the surfaces was largely uniform.

Determination of evanescent field depth using a prism

Laser angles of incidence were measured by placing a 45-45-90^o glass prism (Edmund Scientific, Tonawanda, NY) on the objective, to couple the laser light and project it onto a nearby target. Snell's Law allowed determination of the angle of incidence of the laser, θ_i, as it exits the objective. This angle, in conjunction with the wavelength (λ) and indices of refraction of glass (n_1, 1.515) and the cell (n_2, 1.38) were used to estimate the characteristic depth

$$Dp = \lambda / 4\pi \, (n_1^2 \sin^2\theta_i - n_2^2)^{1/2}.$$

Epifluorescent and confocal imaging

Sensitized emission FRET stoichiometry with epifluorescence illumination was performed as previously described (3-5). Confocal microscopy was performed on cells cultured and transfected on glass coverslips and imaged using an Olympus FV500.

Granule tracking and time-lapse FRET analysis

Granule tracking was performed using MATLAB scripts modified from those in (6). Granules were tracked from CIDA images registered with CIDD and CIAA images via affine transformation. Granules were detected by applying a binary mask to each image, with the masking threshold set to 15 standard deviations above the mean of a background region of interest. This threshold was chosen as it was well above the noise level and detected granules reliably based on visual inspection. The centroid coordinates of each granule in each masked image were determined. Granule centroids were compared across images to determine which granules in each frame had newly appeared, and which had remained from the previous frame. Limits were set for acceptable changes in x-y position and minimum time spent at a position for a given granule to be considered the same. From this analysis, a list of all unique granules in the movie was generated. A more stringent granule tracking procedure was then applied, where each granule was individually tracked starting from the first frame in which it appeared. A 2D Gaussian fit of the granule in its first frame was carried out, and a 12x12 pixel region surrounding the granule's fitted center coordinates was searched in the next frame for a similar Gaussian fit. The best fit within the region was that with the closest match to the Gaussian fits of the granule in the previous frame, based on intensity, half-width, and x-y position. If no Gaussian fit was found, tracking for that granule was terminated. Otherwise, the best matching Gaussian fit was used to search for the granule in the subsequent frame. Granule tracking was terminated if two unique granules collided.

To determine the FRET values for each granule as it was tracked over time, the granule center coordinates in each frame were used to center a 3x3 pixel mask on the CIDD, CIDA, and CIAA images. Mean CIDD, CIDA, and CIAA intensity values within this mask were used to calculate the FRET indices for that granule, using the equations above. ED, EA, Ratio, and x-y coordinates were aligned for all tracked granules of each cell before averaging. The timepoint at which "responder" granules disappeared following application of the elevated K^+ stimulus was set to time = 0. FRET indices were aligned by time prior to disappearance for each responder. "Non-responder" granules were aligned to similar time points as responders from each cell and averaged.

Mathematical simulation of TIR-FRET

To compare our TIR-FRET results to theoretical expectations based on illumination from an exponentially decaying evanescent field, we developed a mathematical model to simulate TIR-FRET. The model used was similar to that described in (3), with the primary exception being that the illumination intensity, rather than being modeled as constant (as would be the case for epifluorescence) was modeled as following a double exponential decay in the z-axis. The two exponentials represent the evanescent field component and a scatter component (see Methods on using silica beads to determine evanescent profile). The relative contributions of the evanescent field and the scatter component were fixed at 85% and 15%, respectively, and the scatter component was fixed as decaying with a depth constant of 1500nm. These values were chosen to approximate those typically measured on our optics, using fluorescent silica beads:

$$I(z) = 0.85e^{-z / Dp} + 0.15\, e^{-z / 1500}$$

Beads and granules were modeled as spheres with diameters of 10μm or 350nm, respectively. The granule diameter of 350nm was chosen to approximate the size of large dense-core granules in neuroendocrine cells (7-9). To simulate a linked FRET probe that localizes to the surface of

the bead/granule, we arbitrarily set the surface concentration (# of molecules per unit area) for both the acceptor and donor equal to 1000. The fraction of donor in complex (fD) was set to 1, and the FRET efficiency (E) for the donor and acceptor was set to 0.4 (the characteristic efficiency of CFP-cYFP in solution (3)). In some cases, a population of free, soluble acceptor molecules was added to this model. Here, the concentration (# molecules per unit volume) was set such that the Ratio of the calculated fluorescence intensity from the bottom of the bead, to the calculated fluorescence intensity of the soluble component outside of the bead, matched the ratio value determined experimentally (ie, the ratio of the fluorescence intensity at the center of the bead footprint, to the fluorescent intensity of the soluble fluorophore in a region clearly outside the bead region, in the CIAA image).

Fluorescence intensities arising from the bead/granule surfaces and from soluble components were determined independently. For fluorescence arising from the surface of a bead/granule, DD, AA, and the sensitized emission FRET signal were modeled as:

$DD_{surface}(x, y, z_1, z_2) =$
$P_1 * [I(z_1) + I(z_2)] * ([\text{donor on surface}] - [\text{bound donor on surface}] * E)$

$AA_{surface}(x, y, z_1, z_2) =$
$P_2 * [I(z_1) + I(z_2)] * [\text{acceptor on surface}]$

$FRET_{surface}(x, y, z_1, z_2) =$
$(\alpha P_2 / \gamma) * [I(z_1) + I(z_2)] * [\text{bound donor on surface}] * E$

The coordinate system used here (x, y, z_1, z_2) depicts the distances of the bottom and top surfaces of the bead/granule from the glass interface (z_1 and z_2, respectively) for a given (x,y) position on the bead/granule. P_1 and P_2 represent the initial intensities (I_o) of the donor and acceptor illuminations, respectively, at the glass-water interface (z = 0). For completeness, fluorescence from both the bottom and top surfaces of the bead at each (x,y) point are taken into account; however, for a 10µm bead, the fluorescent arising from the top surface of the bead was negligible due to the large size of the bead.

Fluorescence intensity arising from the soluble acceptor was determined for each (x, y, z_1, z_2) point, as separate components arising from below the bottom surface of the bead/granule, and above the top surface of the bead/granule:

$$AA_{soluble}(x, y, z_1, z_2) = (P_2 * \int_0^{z_1} I(z) * [\text{soluble acceptor}]) + (P_2 * \int_{z_2}^{\infty} I(z) * [\text{soluble acceptor}])$$

In this model, the total DD and FRET fluorescence originated from the surface of the bead, whereas the total AA fluorescence signal at each (x,y) point was calculated as the sum of $AA_{surface}$ and $AA_{soluble}$ at each (x,y) position.

The fluorescence intensities determined above were then used in conjunction with the FRET stoichiometry equations to calculate the expected values of EA, ED, and Ratio. The FRET calibration constants used for these calculations were taken from the averaged values of the constants over the first 525nm in z, measured from experiments that best approximated the situation being modeled (eg, same characteristic TIRF depth). Note that in order to use the experimentally determined FRET calibration parameters in this model, P_2 was held constant at the arbitrary value of 100, and ratio of P_1 to P_2 was adjusted for each set of constants used, such that EA, ED, and Ratio reported the expected theoretical FRET values (EA = ED = 0.4; Ratio =

1) when only bead/granule surface fluorescence (ie, no soluble fluorophore) was taken into account.

Human Growth Hormone secretion assay

MIN6 cells were plated onto 24-well plates and co-transfected with human growth hormone (hGH) alone or with wild-type, fluorophore-tagged, and mutant forms of Rab27A or Slp4A. The total DNA concentration was held constant across treatments, by addition of a neomycin control plasmid. At 48 hours post-transfection, cells were rinsed for 6 minutes in a physiological saline solution (PSS,145mM NaCl, 5.6mM KCl, 15mM NaHEPES, 0.5mM $MgCl_2$, 2.2mM $CaCl_2$, 2mM glucose, 0.5mM ascorbate, 2mg/ml bovine serum albumin (BSA), pH 7.3), followed by a 6 minute stimulation with PSS containing 70 mM K^+ (equimolar substitution of increased K^+ for Na^+). PSS containing the secreted hGH was collected, and cells were lysed (lysis buffer: 0.2mM EDTA, 10mM HEPES, 1% Triton X-100, pH 7.4) to determine percent of total hGH content secreted. hGH content was measured using an hGH ELISA kit (Roche Diagnostics, Indianapolis, IN).

Statistics

Statistical analyses were performed using GraphPad Prism 5 software (GraphPad Software, La Jolla, CA). For most comparisons *t* tests were used (paired or unpaired), although testing among multiple treatments used ANOVA with post-hoc analysis. Statistical significance was designated at a $p < 0.05$.

REFERENCES

1. Rizzo, M. A., G. H. Springer, B. Granada, and D. W. Piston. 2004. An improved cyan fluorescent protein variant useful for FRET. Nat. Biotechnol. 22:445-449.
2. Griesbeck, O., G. S. Baird, R. E. Campbell, D. A. Zacharias, and R. Y. Tsien. 2001. Reducing the Environmental Sensitivity of Yellow Fluorescent Protein. MECHANISM AND APPLICATIONS. J. Biol. Chem. 276:29188-29194.
3. Hoppe, A., K. Christensen, and J. A. Swanson. 2002. Fluorescence resonance energy transfer-based stoichiometry in living cells. Biophys. J. 83:3652-3664.
4. D'Andrea-Merrins, M., L. Chang, A. D. Lam, S. A. Ernst, and E. L. Stuenkel. 2007. Munc18c interaction with syntaxin 4 monomers and SNARE complex intermediates in GLUT4 vesicle trafficking. J. Biol. Chem. 282:16553-16566.
5. Liu, J., S. A. Ernst, S. E. Gladycheva, Y. Y. Lee, S. I. Lentz, C. S. Ho, Q. Li, and E. L. Stuenkel. 2004. Fluorescence resonance energy transfer reports properties of syntaxin1A interaction with Munc18-1 in vivo. J. Biol. Chem.
6. Yizhar, O., and U. Ashery. 2008. Modulating Vesicle Priming Reveals that Vesicle Immobilization Is Necessary but not Sufficient for Fusion-Competence. PLoS ONE 3:e2694.
7. Winkler, H., and E. Westhead. 1980. The molecular organization of adrenal chromaffin granules. Neuroscience 5:1803-1823.
8. Oheim, M., D. Loerke, W. Stuhmer, and R. H. Chow. 1998. The last few milliseconds in the life of a secretory granule. Docking, dynamics and fusion visualized by total internal reflection fluorescence microscopy (TIRFM). Eur. Biophys. J. 27:83-98.

9. Parsons, T. D., J. R. Coorssen, H. Horstmann, and W. Almers. 1995. Docked granules, the exocytic burst, and the need for ATP hydrolysis in endocrine cells. Neuron 15:1085-1096.
10. Yi, Z., H. Yokota, S. Torii, T. Aoki, M. Hosaka, S. Zhao, K. Takata, T. Takeuchi, and T. Izumi. 2002. The Rab27a/granuphilin complex regulates the exocytosis of insulin-containing dense-core granules. Mol. Cell. Biol. 22:1858-1867.
11. Coppola, T., C. Frantz, V. Perret-Menoud, S. Gattesco, H. Hirling, and R. Regazzi. 2002. Pancreatic beta-cell protein granuphilin binds Rab3 and Munc-18 and controls exocytosis. Mol. Biol. Cell 13:1906-1915.
12. Fukuda, M., E. Kanno, C. Saegusa, Y. Ogata, and T. S. Kuroda. 2002. Slp4-a/granuphilin-a regulates dense-core vesicle exocytosis in PC12 cells. J. Biol. Chem. 277:39673-39678.
13. Gomi, H., S. Mizutani, K. Kasai, S. Itohara, and T. Izumi. 2005. Granuphilin molecularly docks insulin granules to the fusion machinery. J. Cell Biol. 171:99-109.
14. Fukuda, M. 2003. Slp4-a/granuphilin-a inhibits dense-core vesicle exocytosis through interaction with the GDP-bound form of Rab27A in PC12 cells. J. Biol. Chem. 278:15390-15396.
15. Kondo, H., R. Shirakawa, T. Higashi, M. Kawato, M. Fukuda, T. Kita, and H. Horiuchi. 2006. Constitutive GDP/GTP exchange and secretion-dependent GTP hydrolysis activity for Rab27 in platelets. J. Biol. Chem. 281:28657-28665.

SUPPLEMENTAL MOVIES

Supplemental Movie 1
MIN6 cells expressing ROAR-S FRET probes stimulated to undergo exocytosis. Movie shows time-lapse imaging of CIDA fluorescence intensity illustrating distinct puncta of fluorescence that represent secretory granules. Appearance of yellow bar indicates application of elevated [K+] stimulus. Responder granules are circled. Frames were acquired at 0.5 Hz.

Supplemental Movie 2
Pseudocolored ED values on granules from supplementary movie 1.

Supplemental Movie 3
Pseudocolored molar Ratio values on granules from supplementary movie 1.

SUPPLEMENTAL FIGURES

Figure S1. Mathematical TIR-FRET simulation of a 10μm bead coated with a linked donor-acceptor FRET probe. Fig. 2a-c in the main text describes the effects of a moving subcellular compartment on FRET measurements, using 10μm beads uniformly coated with fluoroprotein and resting on a glass coverslip. Each point on the bead footprint image represented fluorescence originating from the bead surface at a specific z-distance from the coverslip. In Fig. S1 we use a mathematical model to simulate TIR-FRET measurements under various conditions. The model is based on that described in (3), with the central difference being that here, the illumination intensity decays exponentially in the z-dimension. We first tested the model by

simulating the experimental conditions from Fig. 2a-c. The concentration of soluble acceptor in the model was adjusted, such that ratios of the maximum on-bead fluorescence intensity (ie, at the very bottom of the bead) to the off-bead fluorescence intensity (ie, determined in a region clearly outside of the bead) calculated by the model matched that determined for each experimental condition. The results of this model are shown in Fig S1a-c. Here, the percentages of off-granule to on-granule fluorescence at z = 0 were 4% (black squares), 11% (green triangles), or 18% (blue circles). Notably, the model accurately matched the shapes and trends of the EA, ED, and Ratio relationships that were measured experimentally (Fig 2a-c), with EA values decreasing, Ratio values increasing, and ED values remaining unchanged with increasing z-distance between the bead surface and the glass coverslip. Moreover, for EA and Ratio, the effects were graded with respect to the concentration of soluble acceptor.

We next modified the TIR-FRET model to simulate how motions of secretory granules might affect TIR-FRET measurements where FRET was localized to the granule. Granules were modeled as spheres (350nm diameter), coated with a linked FRET probe, and surrounded by a solution containing soluble acceptor. The same 3 concentrations of soluble acceptor as in Fig. 2a-c and Figs S1a-c were modeled here (percentages of off-granule to on-granule fluorescence at z = 0 were 4% (black squares), 11% (green triangles), or 18% (blue circles)). The distance between the bottom of the granule and the glass coverslip was varied, and the apparent FRET measurements were calculated through the center of the granule (from the bottom-most to top-most points on the granule). The results of the simulation for EA and Ratio are shown in Figs S1d and e, respectively. ED remained constant at 0.4 (the Ec value of the construct), regardless of the granule's z-position (data not shown). The characteristic TIRF depth of donor and acceptor excitation lines were matched at either 170nm (filled symbols) or 270nm (open symbols).

Figure S2. Validation of sensitized emission TIR-FRET of a plasma membrane localized probe in living MIN6 cells. A linked cYFP-cerulean FRET probe was targeted to the plasma membrane by fusion to the pleckstrin homology (PH) domain of PLCδ. TIR-FRET images were taken of cells expressing the linked-PH probe either alone, or in addition to soluble cerulean or soluble cYFP. (a) Representative CIDA fluorescence image (top) with pseudocolored images of calculated FRET indices (lower) of MIN6 cells transfected with plasmids expressing linked-PH alone (left), or in addition to soluble cerulean (middle) or soluble cYFP (right). The image in the right column shows two adjacent cells that exhibit different fluoroprotein expression levels. Pseudocolor scale is given below images. (b) Averaged fraction of acceptor in complex, (c) donor in complex, and (d) molar Ratio, determined from cells expressing linked-PH only (left), or in addition to soluble cerulean (middle) or soluble cYFP (right). (e) Fraction of donor (fD, circles) or acceptor (fA, triangles) in complex vs molar Ratio, plotted for individual MIN6 cells expressing linked-PH and soluble cerulean. The solid line indicates the linear fit for the fD vs. Ratio data. (f) Same as (e), but for MIN6 cells expressing linked-PH and soluble cYFP. Here, the solid line represents the linear fit of the fA vs. Ratio data. Note that cells expressing the linked-PH probe alone correctly show fA = fD = 1, and Ratio = 1 (b-d). As expected, cells expressing the linked-PH probe with soluble cerulean demonstrate a decrease in fD, no change in fA, and an increase in the molar Ratio on average. Importantly, there is a linear relationship between fD and Ratio, while the fA values remain scattered around 1 (e). These data demonstrate the validity of using sensitized emission TIR-FRET in cells where the FRET is localized to the plasma membrane. FRET stoichiometry calibration constants were obtained

using cerulean-PH (for β), cYFP-PH (for α), and linked-PH (for γ and ξ); 440nm and 514nm lines were matched at Dp = 160nm, as used for experimental data. Bars represent the mean ± SEM. The number of cells used for each condition was: Linked-PH (12); Linked-PH + cerulean (14); Linked-PH + cYFP (11).

Figure S3.

To test the biological function of the ROAR-S FRET probes in the regulated secretory pathway of MIN6 cells, we compared secretory responsiveness of control (hGH only) transfected cells with those overexpressing hGH and FRET probes. Human growth hormone (hGH) secretion induced in response to application of elevated K^+ was assayed as a selective reporter of secretion from transfected cells (Fig. S3a; bars represent the mean ± SEM, with n given above the bars). Previous reports had demonstrated that Slp4A(wt) inhibits secretory responsiveness in PC-12 and insulin secreting cells (10-13). This inhibitory effect results from binding to Rab27A-GDP, as the Slp4A(AG) mutant, which has selectively lost binding to Rab27A-GDP, does not inhibit evoked secretion (14). Importantly, our hGH results are consistent with previous findings, and demonstrate that overexpression with cYFP-Slp4A(wt) results in a 50% reduction in evoked secretion, whereas normal secretion occurred on overexpression with cYFP-Slp4A(AG). Our results also demonstrate that secretory responses in cells overexpressing unlabeled Rab27A and fluorophore-labeled Rab27A do not differ significantly from control secretory responses in cells expressing hGH alone. In contrast, overexpression of the dominant negative CFP-Rab27A(T23N) construct resulted in an approximate 50% inhibition of stimulated hGH secretion compared to control. Considered together, these data demonstrate that the FRET probes used here retain normal biological function with respect to the regulated secretory pathway when overexpressed in MIN6 cells.

Importantly, confocal fluorescence imaging demonstrated that CFP-Rab27A(wt), cYFP-Slp4A(AG), and NPY-Cherry (a luminal marker of insulin-containing granules) overlapped in localization when co-expressed in MIN6 cells, reflecting the endogenous distribution of Rab27A and Slp4A on secretory granules (Fig. S3b) (10, 12). (Expression of single fluoroproteins demonstrated complete spectral separation under our confocal imaging conditions). Most of the fluorescent Rab27A donor was granule localized, as average off-granule to on-granule fluorescence ratio of Rab27A was measured to be ~13.4% ± 1.5%. This suggests an upper limit of 86% of Rab27A to be in the GTP-bound state, a value similar to a previously reported 74% of cellular Rab27A existing in the GTP bound state in human platelets (15).

To establish the specificity of our FRET assay, we co-expressed combinations of FRET probes in MIN6 cells, and measured the resulting sensitized emission FRET under epifluorescent illumination (Fig S3c-e; bars represent the mean ± SEM, with n, given above the bars). At a molar Ratio range of 0.9-1.1, equivalent apparent FRET efficiencies were measured between cYFP-Slp4A(wt) and both the active(Q78L) and inactive(T23N) CFP-Rab27A mutants, consistent with the finding that Slp4A(wt) binds Rab27A-GTP and -GDP equally (Fig. S3c). Importantly, the cYFP-Slp4A(AG) mutant exhibited FRET with CFP-Rab27A(wt) and the active CFP-Rab27A(Q78L), but not with the inactive CFP-Rab27A(T23N) at a molar Ratio range of 0.9-1.1, consistent with the finding that Slp4A(AG) selectively binds activated Rab27A (Fig. S3d). Here, the dashed line in Fig. S3c-d indicates the baseline level of the FRET assay, as measured in cells co-expressing soluble CFP and cYFP. Notably, the FRET efficiency was found to be higher for the Rab27A(wt)-Slp4A(AG) interaction than for the Rab27A(Q78L)-Slp4A(AG) interaction when compared at a 0.9-1.1 molar Ratio range (Fig. S3d). When the

FRET efficiency was measured in cells that spanned an extended molar ratio range, both Rab27A(wt) and the Q78L mutant achieved the same FRET efficiency at high molar ratios, while the T23N mutant lagged considerably (Fig. S3e). These results are consistent with the Rab27A(Q78L) mutant exhibiting a lower affinity for Slp4A relative to its wt counterpart.

Figure S4.

One advantage of using the FRET stoichiometry analysis for our TIR-FRET approach is that, in addition to measurement of apparent FRET efficiencies, the analysis also yields the molar Ratio of acceptor to donor, as well as the total acceptor fluorescence and total donor fluorescence. As such, our TIR-FRET approach can be used to monitor the relative cycling of donor and acceptor proteins on and off of subcellular compartments. Fig. S4 demonstrates the time course of normalized (a) total acceptor intensity (514nm excitation), (b) total donor intensity (442nm excitation, in addition to the calculated donor fluorescence that was quenched due to FRET), and (c) molar Ratio prior to granule disappearance, for responder granules (blue circles) and non-responder granules (green triangles). Data for non-responders were aligned to similar time points as responders from each cell and averaged. Total acceptor and donor intensities for each granule were normalized to the corresponding intensity at the time point immediately prior to fusion. Data represent the mean ± SEM (n=10 cells/32 responders/202 non-responders).

Notably, the total fluorescence intensities of both donor and acceptor fluoroproteins decreased on responder granules, while the molar Ratio remained unchanged. While one might conclude from this that responder granules are simply moving away from the plasma membrane, our mathematical modeling suggests otherwise. If the decrease of granule-localized acceptor (~30%) is considered as representing axial movement away from the plasma membrane, then it would represent an axial movement of ~60 nm (for Dp = 170nm, as used in the experiment). By comparison to the observed increase in ED, our mathematical simulation of the experimental conditions demonstrates that, in the absence of any change in molecular interaction, a simple axial movement of a granule away from the plasma membrane would result in a decrease in measured ED. Moreover, our model estimates that movement of a granule *away* from the plasma membrane, from z-distance of 0 to 60 nm, would result in a ~2% decrease in FRET (given Dp = 170nm). Conversely, our model predicts that movement of the granule towards the plasma membrane (from z-distance of 60 nm to 0 nm), would result in a ~ 2% increase in FRET. Importantly, these minimal changes in FRET seen with axial movement cannot account for the 30% increase in FRET that we observed in our experiments.

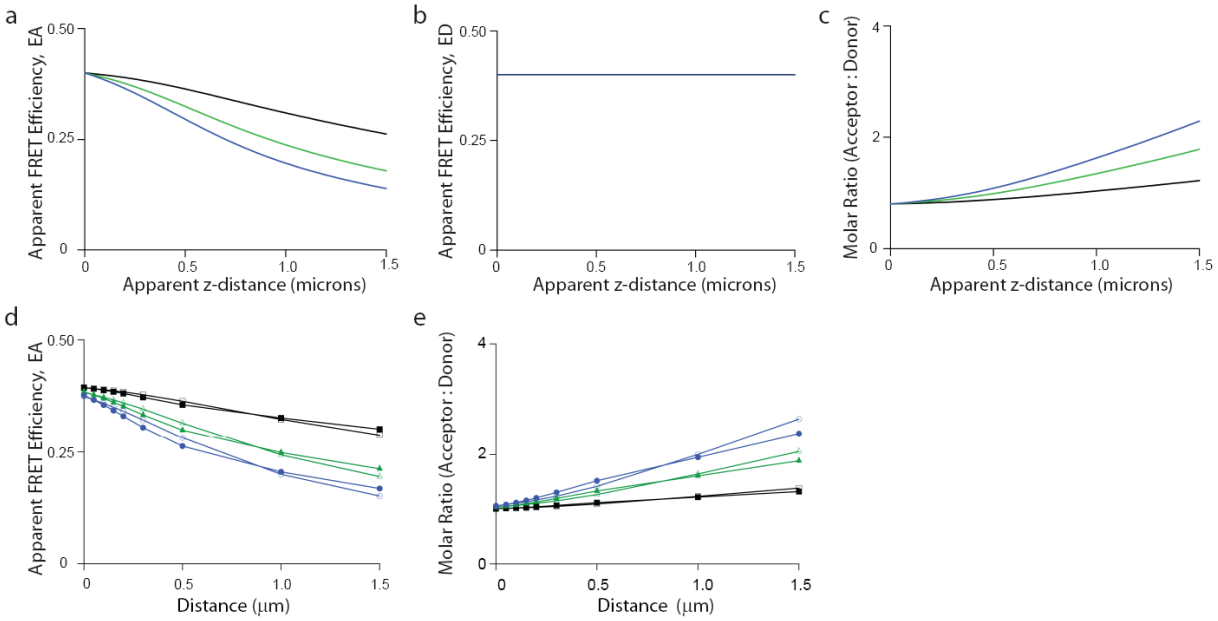
a
Apparent FRET Efficiency, EA
0.50
0.25
0
0
0.5
1.0
1.5
Apparent z-distance (microns)
b
Apparent FRET Efficiency, ED
0.50
0.25
0
0
0.5
1.0
1.5
Apparent z-distance (microns)
c
Molar Ratio (Acceptor : Donor)
4
2
0
0
0.5
1.0
1.5
Apparent z-distance (microns)
d
Apparent FRET Efficiency, EA
0.50
0.25
0
0
0.5
1.0
1.5
Distance (μm)
e
Molar Ratio (Acceptor : Donor)
4
2
0
0
0.5
1.0
1.5
Distance (μm)

Fig. S1

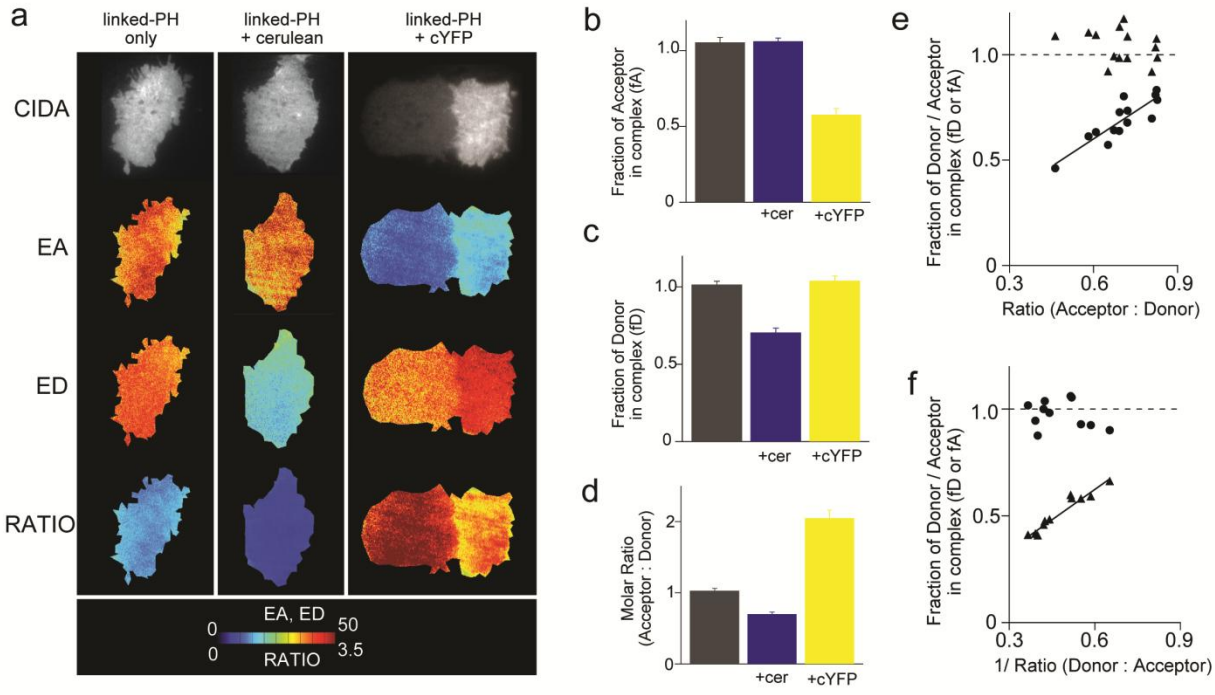
a
linked-PH only
linked-PH + cerulean
linked-PH + cYFP
CIDA
EA
ED
RATIO
EA, ED
0
50
0
3.5
RATIO
b
Fraction of Acceptor in complex (fA)
1.0
0.5
0
+cer
+cYFP
c
Fraction of Donor in complex (fD)
1.0
0.5
0
+cer
+cYFP
d
Molar Ratio (Acceptor : Donor)
2
1
0
+cer
+cYFP
e
Fraction of Donor / Acceptor in complex (fD or fA)
1.0
0.5
0
0.3
0.6
0.9
Ratio (Acceptor : Donor)
f
Fraction of Donor / Acceptor in complex (fD or fA)
1.0
0.5
0
0.3
0.6
0.9
1/ Ratio (Donor : Acceptor)

Fig. S2

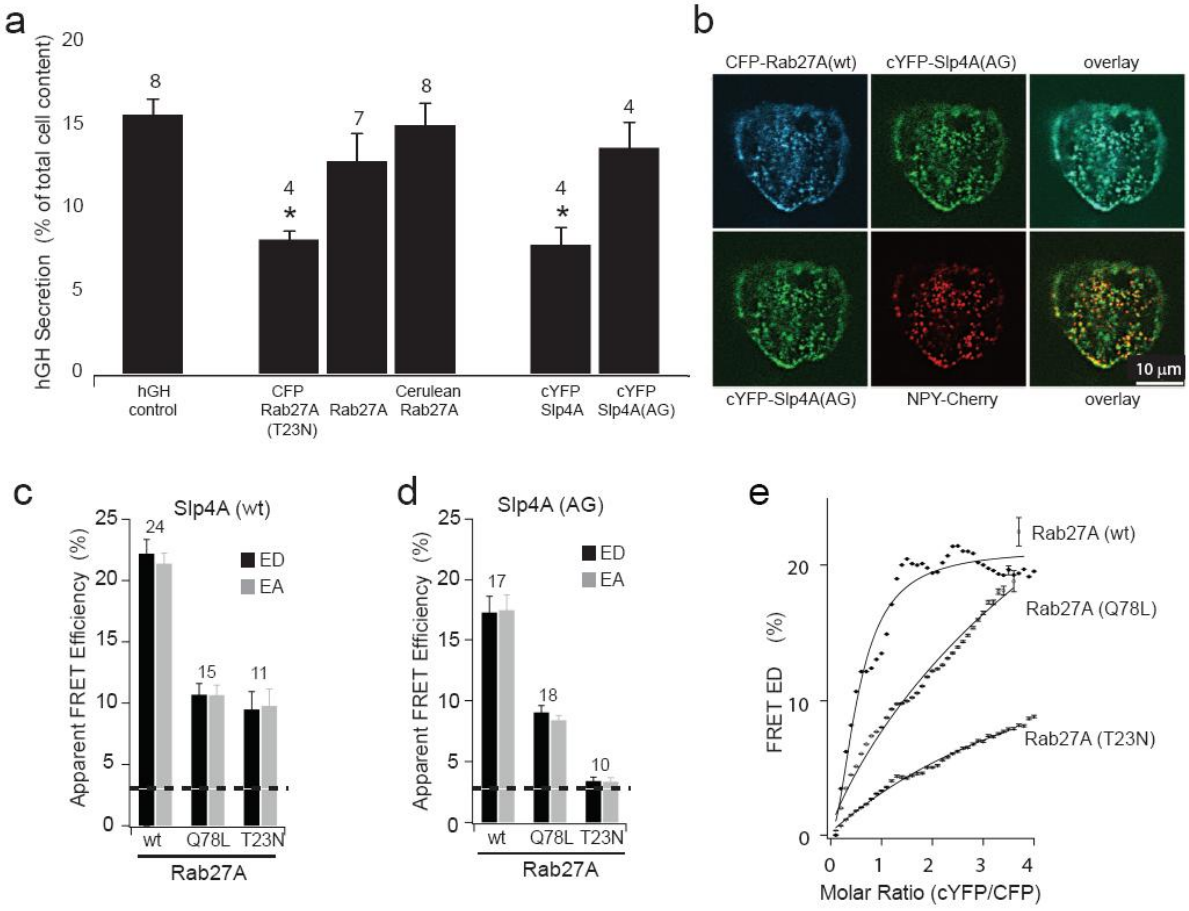
a
hGH Secretion (% of total cell content)
20
15
10
5
0
8
4
*
7
8
4
*
4
hGH control
CFP Rab27A (T23N)
Rab27A
Cerulean Rab27A
cYFP Slp4A
cYFP Slp4A(AG)
b
CFP-Rab27A(wt)
cYFP-Slp4A(AG)
overlay
10 µm
cYFP-Slp4A(AG)
NPY-Cherry
overlay
c
Slp4A (wt)
Apparent FRET Efficiency (%)
25
20
15
10
5
0
24
15
11
ED
EA
wt
Q78L
T23N
Rab27A
d
Slp4A (AG)
Apparent FRET Efficiency (%)
17
18
10
ED
EA
wt
Q78L
T23N
Rab27A
e
FRET ED (%)
20
10
0
Rab27A (wt)
Rab27A (Q78L)
Rab27A (T23N)
0
1
2
3
4
Molar Ratio (cYFP/CFP)

Fig. S3

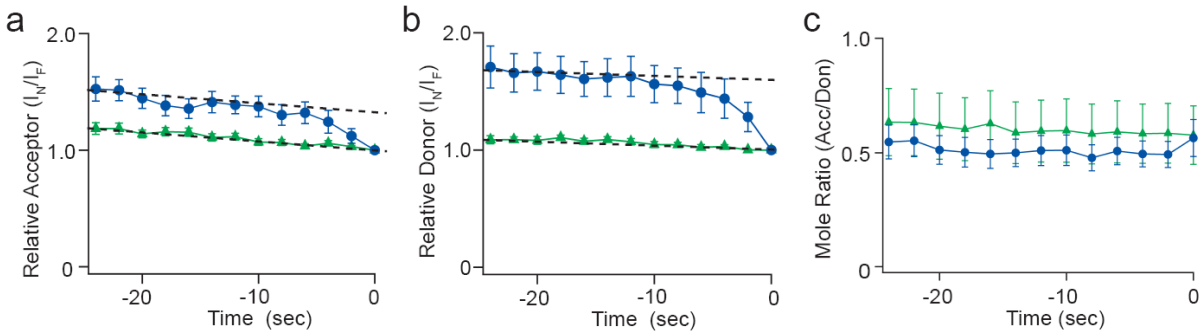
a
Relative Acceptor (I_N/I_F)
2.0
1.0
0
-20
-10
0
Time (sec)
b
Relative Donor (I_N/I_F)
2.0
1.0
0
-20
-10
0
Time (sec)
c
Mole Ratio (Acc/Don)
1.0
0.5
0
-20
-10
0
Time (sec)

Fig. S4